



Numerical investigation on the implications of spring temperature and discharge rate with respect to the geothermal background in a fault zone

Zhenjiao Jiang¹ · Tianfu Xu¹ · Gregoire Mariethoz²

Received: 16 October 2017 / Accepted: 30 March 2018
© Springer-Verlag GmbH Germany, part of Springer Nature 2018

Abstract

Geothermal springs are some of the most obvious indicators of the existence of high-temperature geothermal resources in the subsurface. However, geothermal springs can also occur in areas of low average subsurface temperatures, which makes it difficult to assess exploitable zones. To address this problem, this study quantitatively analyzes the conditions associated with the formation of geothermal springs in fault zones, and numerically investigates the implications that outflow temperature and discharge rate from geothermal springs have on the geothermal background in the subsurface. It is concluded that the temperature of geothermal springs in fault zones is mainly controlled by the recharge rate from the country rock and the hydraulic conductivity in the fault damage zone. Importantly, the topography of the fault trace on the land surface plays an important role in determining the thermal temperature. In fault zones with a permeability higher than 1 mD and a lateral recharge rate from the country rock higher than 1 m³/day, convection plays a dominant role in the heat transport rather than thermal conduction. The geothermal springs do not necessarily occur in the place having an abnormal geothermal background (with the temperature at certain depth exceeding the temperature inferred by the global average continental geothermal gradient of 30 °C/km). Assuming a constant temperature (90 °C here, to represent a normal geothermal background in the subsurface at a depth of 3,000 m), the conditions required for the occurrence of geothermal springs were quantitatively determined.

Keywords Geothermal spring · Fault hydrogeology · Numerical modeling · Groundwater flow

Introduction

Geothermal energy is a clean and renewable energy source that has been exploited to generate electricity, as well as being widely used for space heating and in heat pumps (Lund et al. 2011). Geothermal energy can originate from the decay of radiogenic elements such as ⁴⁰K, ²³²Th, and ²³⁸U within the upper crust, or from recent magmatic episodes in association with heat input from the Earth's mantle (Boyle 1997). Heat transfers from the Earth's interior toward the surface by heat

conduction and convection, causing an increase of subsurface temperature with depth. The average geothermal gradient of the continental crust is roughly 30 °C/km, but it varies significantly in space (Chapman 1986). In some areas, the thermal gradient can be much greater than the average gradient, which leads to thermal anomalies in the subsurface, and may result in surface manifestations, typically geothermal springs. These thermal anomalies can relate to the intrusion of magma into the shallow crust or, upwelling of heat and/or fluids from the crust-mantle boundary. The heat transport from the deep subsurface can be influenced or modified in a number of ways—for example, upward convective transport can be slowed by the presence of low-permeability cap rock (Mádli-Szőnyi and Tóth 2015), resulting in the accumulation of heat in a geothermal reservoir, or conductive faults may provide conduits that concentrate heat and fluid flow, potentially transporting them to the surface (Bucher et al. 2009; Christensen and Mooney 1995).

Geothermal springs are the primary geothermal signal attracting further geothermal exploration and exploitation;

✉ Zhenjiao Jiang
jiangzhenjiao@hotmail.com

¹ Key Laboratory of Groundwater Resources and Environment, Ministry of Education, College of Environment and Resources, Jilin University, Changchun 130021, China

² Institute of Earth Surface Dynamics, University of Lausanne, 1015 Lausanne, Switzerland

however, before drilling can begin, the location of hot fluid reservoirs must be predicted (Younger 2014). Disappointedly, low subsurface temperatures are often encountered in areas where geothermal springs occur. This phenomenon raises two questions: (1) under what conditions do geothermal springs occur and (2) if a geothermal spring is observed, is it an indication of high-temperature geothermal anomalies in deep subsurface. Considering that the occurrence of geothermal springs is commonly related to the existence of faults (Curewitz and Karson 1997; Stober et al. 2016), this study involves a quantitative analysis of the conditions for the occurrence of geothermal springs in a fault zone, and analyzes its implications for the geothermal background in the subsurface. While there is no universally accepted definition for the geothermal spring (it can be defined as outflowing water temperature above human body temperature or with temperatures above its surroundings or mean air temperature (Judson et al. 1987; Pentecost et al. 2003), the authors here consider that a spring with the temperature higher than the mean air temperature in summer (30 °C, in China) is a geothermal spring. It is also considered that a temperature in the subsurface that is higher than calculated by the average geothermal gradient of continental crust indicates a geothermal anomaly in the subsurface.

The heat and fluid transport controlled by faults has been studied widely. These studies either focus on heat and flow processes within the fault damage zone (e.g. Fairley and Hinds 2004; Malkovsky and Magri 2016; Murphy 1979), or investigate the influence of faults (permeable or impermeable, heterogeneous or homogeneous, isotropic or anisotropic) on the regional flow and temperature in a two-dimensional (2D) or three-dimensional (3D) sense (e.g. Ball et al. 2014; Fairley 2009; Forster and Smith 1989; Karrech et al. 2014; López and Smith 1995; Saffer et al. 2003; Smith 1980). In 3D models, faults can be embedded in country rocks, where the country rock is assumed to be impermeable relative to the fault zone (Malkovsky and Magri 2016; Sorey 1975) or as having a homogeneous permeability to influence the geothermal processes in the fault zone (Ji et al. 2016; López and Smith 1995; Magri et al. 2016). With 3D models, the effect of faults is often underestimated because the size of the fault damage zone is far smaller than the size of the country rock formation, and it is difficult to fully incorporate both the country rock and narrow fault zone in the same 3D numerical model. Alternatively, 2D models are often used to simulate the heat and flow processes affected by the fault in great detail (Bense et al. 2013).

Most 2D models represent a cross-section of the country rock, conceptualizing the fault as a 1D feature that alters the permeability of the country rock. These models are able to recreate the geothermal spring formed by the water flowing through the country rock, and after heating, migrating upwards along fault damage zone (e.g. Bense and Person 2006). However, in zones made of crystalline rocks or low-

permeable sedimentary rocks, the formation of geothermal springs can be conceptualized as water and heat transport in the fault damage zone, with limited lateral recharge from surrounding rocks. This happens for example in the Hot Creek near Mammoth, California, USA (Sorey 1985) and also in the northeastern Tibetan Plateau, e.g. Zhacang geothermal spring in the Guide Basin, China (Jiang et al. 2018).

To study such geothermal systems, a 2D model of a hydraulically conductive fault zone is established, and the influence of the fault geometries and properties on the spring temperature and discharge rate is quantitatively analyzed. The contribution of water from the country rock is defined in terms of its role as the source of water entering the fault plane. Based on multiple numerical models, a database is established including spring temperatures under different scenarios of hydraulic conductivity, the lateral recharge rate from the country rock, and the distance between circulation depth and the 90 °C line. This database can be used to infer the geothermal background in the subsurface from the spring temperature and discharge rate.

Model setup

Geometry

This study considers the common case of a conductive fault formed in the country rock (Fig. 1a). The rock within the fault damage zone is more easily eroded, creating a valley and stream along the fault trace on the land surface. The fault cannot extend infinitely, but ends at a certain length in igneous or sedimentary rocks, or at the position intersecting other impermeable structures such as a tilted low-permeability reverse fault after multiple-phase tectonic activities (Fig. 1a; e.g. Barka and Kadinsky-Cade 1988; Peacock and Sanderson 1992; Wibberley et al. 2008). The formation of geothermal springs is related to the flow and heat transport in the fault damage zone, with the water recharging from the high-elevation positions along the fault trace and discharging at low-elevation positions. The discharge rate and temperature of the thermal spring can be affected by lateral recharge from the country rock. To determine the controlling factors of the temperature and discharge rate of a geothermal spring, the conductive fault (blue part in Fig. 1a) was extracted from the country rock, and was described by the fault length, depth, slope of the fault trace and the intersection angle between conductive fault and impermeable structure (Fig. 1b). A 2D numerical model was then built on this conductive fault.

Boundary conditions

In the numerical model, the fixed water heads are defined on the fault top, which is assumed to be equal to the elevations

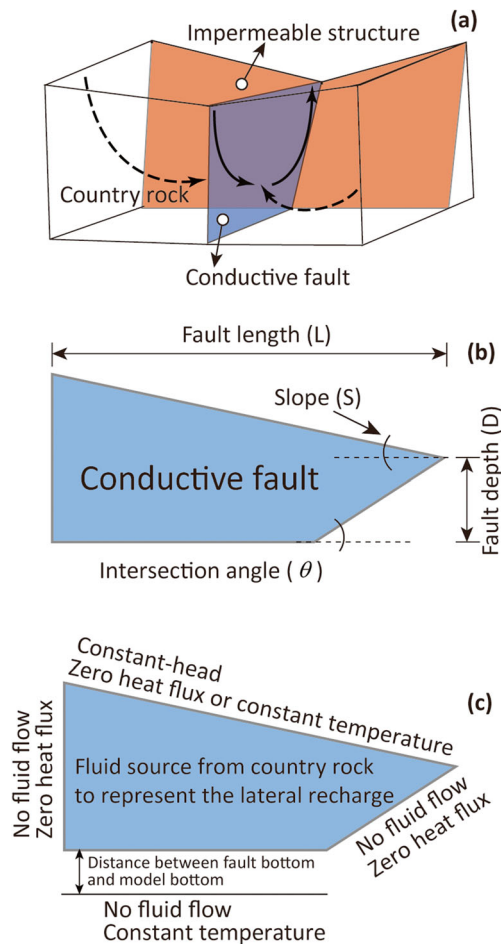


Fig. 1 **a** Conceptual model of a conductive fault embedded in country rock and terminated by an impermeable structure, with water entering the conductive fault from the country rock in any direction and flowing through the fault to form springs, **b** the model domain focusing on the conductive fault, with the geometry described by the fault depth, fault length, intersection angle between the conductive fault and impermeable structure (which can represent for example the dip angle of the impermeable structure), and the slope of the fault trace on the land surface, **c** the heat and flow boundary conditions used in the numerical model

along the fault trace, representing the free water table when the fault zone is saturated and a stream occurs along the fault (López and Smith 1995). This allows the fault trace to behave as either a recharge or a discharge location, depending on the lateral recharge rate from the country rock (Fig. 1a). The properties of recharge or discharge adjust dynamically in the numerical model. The water flow induced by the slope of the water table along the conductive fault is here referred to as topography-driven flow. The discharge rate at the positions with low elevation along the fault is therefore composed by two parts: the topography-driven flow from the upstream zone of the conductive fault and the lateral recharge from the country rock.

In the 2D model, the hydraulic head in the fault is assumed to be lower than that in the country rock. The lateral recharge

from the country rock is evenly assigned on the conductive fault profile, without considering its vertical variation related to the heterogeneous permeability distribution in the country rock and conductive fault (López and Smith 1995). The role of this averaged lateral recharge is defined by the internal water source at each cell in the model domain, which has a temperature equal to that of the previous time step at each inflow position. The influence of the country rock is therefore included, although the 2D model is established on the conductive fault; however, the detailed pathways of the water flow in the country rock were not considered. In addition, the flow via the fault bottom and both sides of the fault zone (left and right sides in Fig. 1c) are assumed to be zero, as the contact area between the conductive fault and the country rock on the bottom and lateral sides is far smaller than that along the fault profile.

On the fault top, a constant temperature (15 °C, mean atmosphere temperature in China) is prescribed at nodes where water enters the fault zone. No heat-transport boundary condition is set at nodes where water leaves the domain, allowing free outflow of the water with the calculated temperature (Diersch 2013). Besides, zero heat exchange is defined on both lateral boundaries at the upstream and downstream ends of the fault, because there is no fluid flow to drive the heat flux and no significant temperature difference at both sides of the lateral boundaries to drive heat conduction. To determine the boundary condition at the fault bottom, an initial model was run, with constant temperature of 15 °C at the model top and constant heat flux of 60 mW/m² (continental average) on the model bottom. A uniform initial hydraulic head was given on the entire fault zone, which means no fluid flow to drive heat transport. A steady-state fluid and heat transport simulation resulted in a temperature of 90 °C along the fault bottom driven by merely heat conduction; thus, a constant temperature of 90 °C at the depth of 3,000 m is assigned to the fault bottom, to represent a normal geothermal background. The resultant temperature and hydraulic head distribution in the fault zone is used as the initial conditions for the later numerical modeling in this work. The rationale of using a constant temperature boundary, rather than the constant heat flux, on the fault bottom is discussed later.

Spatial and temporal discretization

The governing equations for heat and flow transport in the fault zone are summarized in the Appendix, and are solved in FEFLOW (Diersch 2013), a well-accepted finite-element modeling package. In the numerical model, the fault zone is discretized into 70,671 triangular elements with cell sizes <10 m. Each simulation is run until the temperature and water head in the fault zone reach steady or quasi-steady state. The magnitude of time steps is varied automatically following the forward Adams-Bash forth/backward trapezoid scheme

(Diersch and Kolditz 2009). The numerical model involves variations of density, viscosity and hydraulic conductivity with the temperature, but the heat capacity and conductivity are assumed to be constant. The temperature and flow rate of the spring and the flow/heat patterns in the conductive fault are discussed with respect to the fault geometry and material properties. The strategies for the simulation are summarized in Table 1.

Results

Mechanism analysis

By adjusting the lateral recharge from the country rock (Q_L) from 1 to 1,000 m³/day or the hydraulic conductivity (K) from 10⁻³ to 10 m/day, and fixing the other parameters in the base case (Table 1), similar flow and temperature patterns are observed in the fault zone (Fig. 2). As shown in Fig. 2b, d, a low-temperature zone appears at the upstream zone of the fault, which is induced by the downward inflow of cold water (15 °C) from the fault top. The temperature increases along the flow path due to heat input from the fault bottom. As a consequence, the geothermal spring forms at the downstream part ($x = 40\text{--}50$ km, Fig. 2a) of the fault when Q_L is 20 m³/day, and the discharge distance expands to $x = 10\text{--}50$ km when Q_L increases to 800 m³/day (Fig. 2c). However, the maximum outflow temperature decreases with Q_L (Fig. 2b, d). An upward fluid flux driven by the density contrast relating to the temperature gradient is also observed in Fig. 2a, c that at the

fault bottom. The direction of heat flux follows the flow velocity, suggesting the dominant control of convection on the heat transport in the fault zone.

The heat transport mechanisms are further investigated in Fig. 3, where the total heat flux in Fig. 3a is separated into three parts: the convection relating to the topography-driven flow (Fig. 3b), the convection relating to the density-driven flow (Fig. 3c), and the heat conduction relating to the temperature gradient (Fig. 3d). Among all these mechanisms, it is clear that the topography-driven convection plays a dominant role in controlling the heat flux in the fault zone. The heat flux at the discharge zone driven by heat conduction (<0.0015 W/m²) is lower than the heat convection (<65 W/m²) by almost four orders of magnitude (Fig. 3b,d). Moreover, the heat flux induced by density contrast (density-driven flow) is critical. At the discharge area, the density-driven heat flux accounts for 31% of the total heat flux, as illustrated in Fig. 3c. This ratio further increases with the system temperature.

The discharge rate of springs along the fault and the maximum spring temperature were then calculated at 29 sets of hydraulic conductivity in the fault zone (K) and lateral recharge from the country rock (Q_L) (Fig. 4c). The distribution of discharge rate and maximum temperature in the K - Q_L domain were interpolated via kriging (Fig. 4), which expresses the relationship between spring temperature, total discharge rate, K and Q_L . It was tested that adding more calculations for other sets of K and Q_L has a negligible influence on the interpolation results. As shown, both discharge rate and maximum temperature are influenced by K and Q_L . However, the outflow temperature does not necessarily decrease or increase

Table 1 The geometry and thermal and hydraulic parameters used in the numerical models, with the *italic* representing the base case

Parameter, symbol	Range	Explanation
Slope of fault trace, S	5%, 1%	e.g. Barka and Kadinsky-Cade (1988), Peacock and Sanderson (1992), Wibberley et al. (2008)
Fault length, L	50, 40, 10 (km)	
Intersection angle, θ	30°, 45°, 90°, 135°	
Fault depth, D	3,500, 3,000, 2,000 (m)	The fault depth varies from 3,500 to 2,000 m, by fixing the temperature of 90 °C at the fault bottom
Distance between fault bottom and 90° line, DT	50, 500, 1,000 (m)	By fixing a temperature of 90 °C at 3,000 m, the distance between the fault bottom and the 90 °C line is adjusted among 50, 500 and 1,000 m. The zone between the fault bottom and 90 °C line has an extremely low permeability and porosity to represent a tight rock
Heat capacity of rocks, C	2.0, 3.0, 4.0 (MJ/m ³ /°C)	Representing the properties of three rocks: shale, sandstone and granite
Thermal conductivity of rocks, λ	1.4, 2.7, 3.5 (W/m/°C)	
Thermal dispersivity, α	50, 100, 150 (m)	Following the grid Peclet number criterion of: $\Delta x/\alpha \leq 2$
Hydraulic conductivity of fault, K	0.001–10, 1 (m/day)	The hydraulic conductivity (K) in FEFLOW here is given at the reference temperature of 15 °C, which corresponds to the permeability of 10 ⁻¹⁵ –10 ⁻¹¹ m ² (Evans et al. 1997). A permeability-porosity relationship is employed (Cappa and Rutqvist 2011, Evans et al. 1997): $k/k_0 = (\phi/\phi_0)^n$, where k is the permeability, ϕ is the porosity, k_0 is a known permeability ($k_0 = 5 \times 10^{-15}$ m ²) corresponding to reference porosity ϕ_0 of 0.03 measured in the laboratory, and n is the index (4.0)
Effective porosity, ϕ	0.03–0.3, 0.17	
Lateral recharge from country rock, Q_L	1–10,000, 20 (m ³ /day)	According to the case studies in López and Smith (1995)

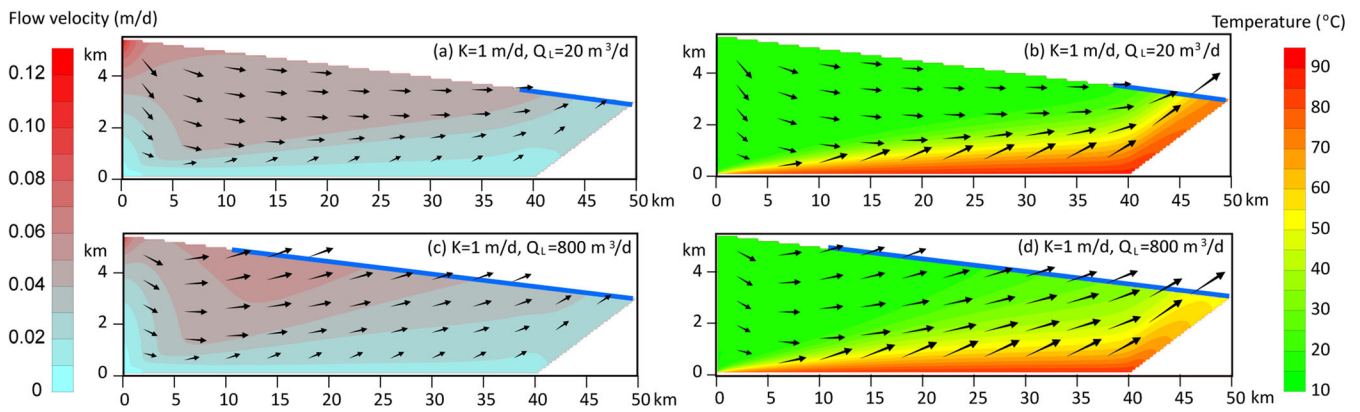


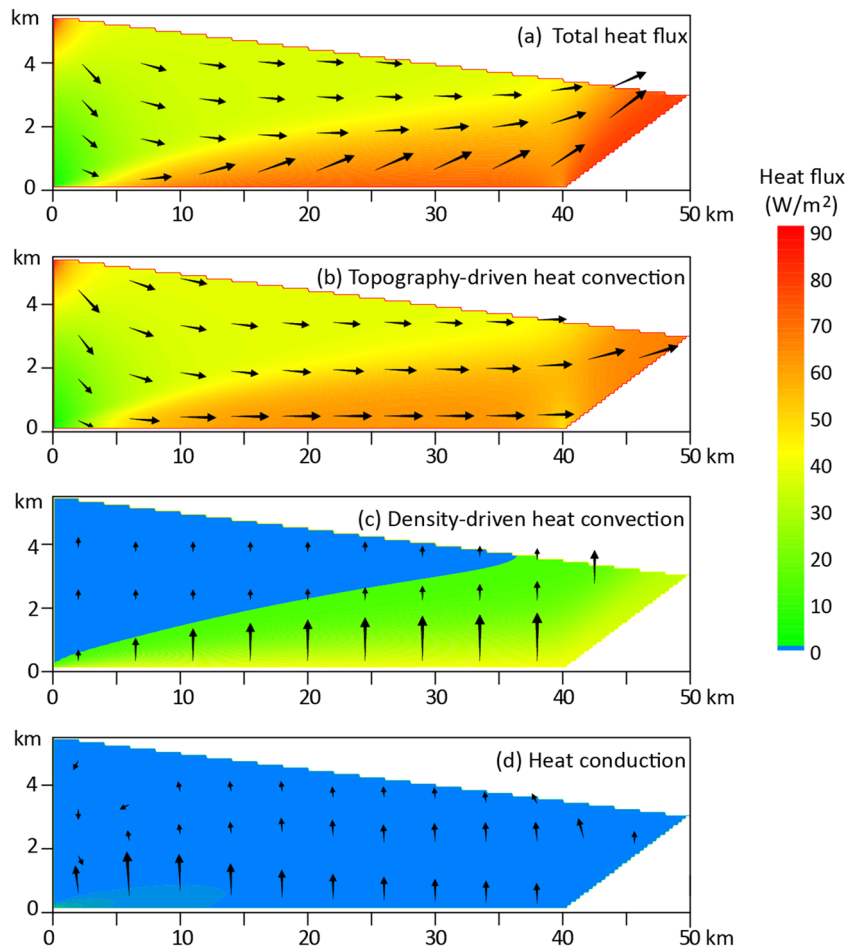
Fig. 2 **a** and **c** The magnitude of flow velocity and flow direction, and **b** and **d** the temperature and heat flux (arrow) distributions in the conductive fault at a lateral recharge rate of 20 and 800 m³/day,

respectively, with topographic slope of 5%. The blue line in each figure indicates the discharge area corresponding to springs

with the discharge rate (Fig. 4a,c), but depends on the components of discharged water (Fig. 4b,c). The K - Q_L domain in Fig. 4a was divided into three major zones according to the ratio of topography-drive flow in the total discharge rate ($Q_{\text{topo}}/Q_{\text{Total}}$; Fig. 4b). In zone I, $Q_{\text{topo}}/Q_{\text{Total}}$ approaches zero, and the discharged water mostly comes from lateral recharge

from the country rock (Q_L). Consequently, discharge rate increases with Q_L , but is weakly affected by K . In zone III where $Q_{\text{topo}}/Q_{\text{Total}}$ is higher than 50%, the discharge water is composed by both lateral recharge from the country rock and topography-driven flow along the fault trace. Under this scenario, the increase in Q_L induces vertical flux in the fault zone,

Fig. 3 **a** The total heat flux calculated at hydraulic conductivity of 1.0 m/day and lateral recharge of 20 m³/day, which is mainly composed by **b** topography-driven heat flux and **c** density-driven heat flux, but weakly affected by **d** heat conduction. The topography-driven heat flux is calculated by neglecting the density-driven flow and conductive heat flow; the density-driven flux is inferred by removing the topography-driven heat flux and conductive heat flux from the total heat-flux. The flux pattern was also calibrated for hydraulic conductivities of 0.001, 0.01 and 0.1 m/day, and the lateral recharge rates of 200 and 1,000 m³/day, where similar patterns were observed



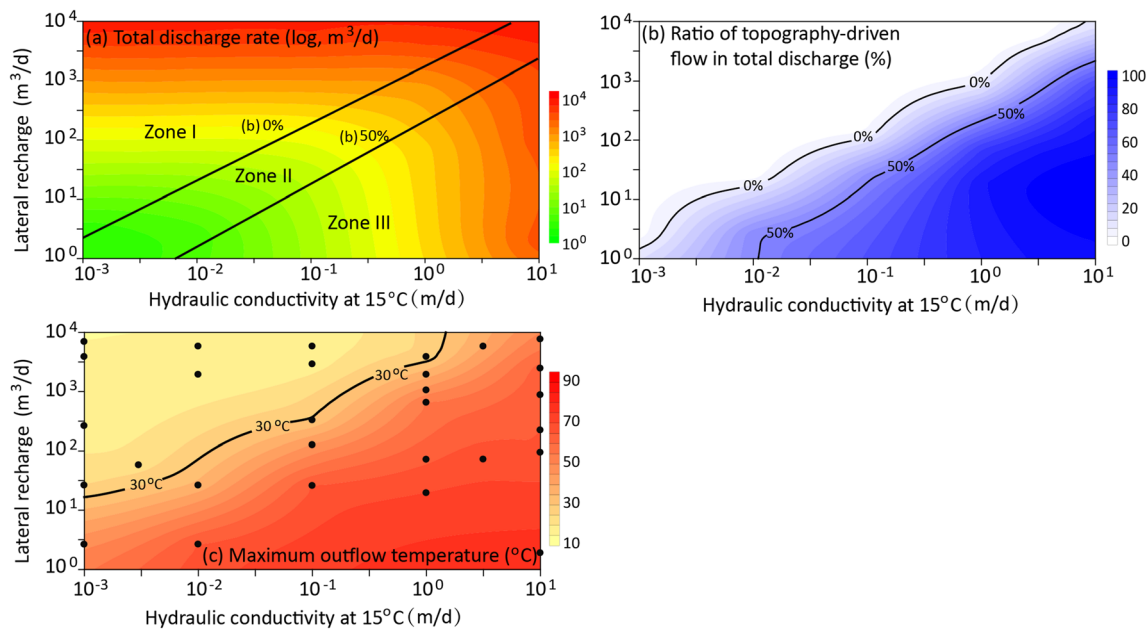


Fig. 4 **a** Discharge rate of springs along the fault trace, **b** ratio of topography-driven flux in the total discharge ($Q_{\text{topo}}/Q_{\text{total}}$), and **c** maximum spring temperature in the K – Q_L domain, where K represents the hydraulic conductivity and Q_L represents the lateral recharge from the

country rock. The black dots represent the simulated scenarios, and the lines of 0 and 50% in **b** are approximately copied to **a** to illustrate the compositions (topography-driven flux versus lateral recharge) in the total discharge rate of the spring

resulting in an increased discharge range along the fault trace (Fig. 2a,c), but a decrease in the topography-driven flow. As a consequence, in zone III, the discharge rate (as the sum of topography-driven flow and the lateral recharge from country rock) does not appear to increase with Q_L . As topography-driven flow depends on K , the discharge rate thus varies with K in zone III. Located between zones I and III, discharge rate in zone II is related to both K and Q_L .

Recalling the flow path in Fig. 2a, the topography-driven flow recharging from the upstream of the fault has a longer flow path and thus a longer interaction period with the heat source at the fault bottom. As a result, maximum spring temperature increases with the ratio of $Q_{\text{topo}}/Q_{\text{total}}$ and K (Fig. 4b,c). In contrast, the increase of Q_L leads to a greater vertical flux, which has a much shorter flow path than that of topography-driven flow; therefore, the maximum spring temperature decreases with the increase of Q_L .

The maximum spring temperature appears to increase with K , but decreases with Q_L (Fig. 4b), because convection controls heat transport in the K and Q_L domain discussed here ($K > 0.001$ m/day and $Q_L > 1$ m³/day; Fig. 3), and the spring temperature is controlled by the residual time of the water in the fault zone. This result is comparable to that of López and Smith (1995), where the relationship of spring temperature with K in both the fault zone and country rock was discussed in a quasi-3D model, by fixing the hydraulic gradient in the country rock. Instead, Q_L is used in this work to represent the effects of both hydraulic conductivity and hydraulic gradient in the country rock on the spring discharge and temperature.

Sensitivity analysis and controlling factor filtering

To define the conditions for the formation of geothermal springs, the contour line with a temperature of 30 °C (CL30) was introduced (Fig. 4c), and the geothermal spring occurs when the K – Q_L values are located below this line. CL30 is then extracted at different fault geometries in Fig. 5. It is shown that CL30 shifts upward when the slope of the fault trace increases from 1 to 5% (Fig. 5a), and the domain of K and Q_L for the geothermal spring occurrence is enlarged. The conditions for geothermal spring occurrence can also relax with the increase of fault length (Fig. 5b) and with the intersection angle between the conductive fault and the low-permeable structure increasing from 30 to 90° (Fig. 5e), which is attributed to the increase of the interaction period for fluid and heat source at the fault bottom to hold more energy. It is found that the intersection angle increasing further from 90 to 135° has a negligible influence on the spring temperature (Fig. 5e), because the water within the bottom-left corner does not significantly contribute to the water circulation in the fault zone.

Importantly, the position of CL30 is not related to the fault depth (Fig. 5c), but is overwhelmingly controlled by the distance between the fault bottom (or circulation depth of spring water) and the 90 °C line (Fig. 5b), which is expressed by DT. The range of K – Q_L for the formation of the geothermal spring decreases dramatically with an increase in DT. When DT is greater than 1,000 m, the geothermal spring with the maximum temperature > 30 °C can only occur for $Q_L < 10$ m³/day

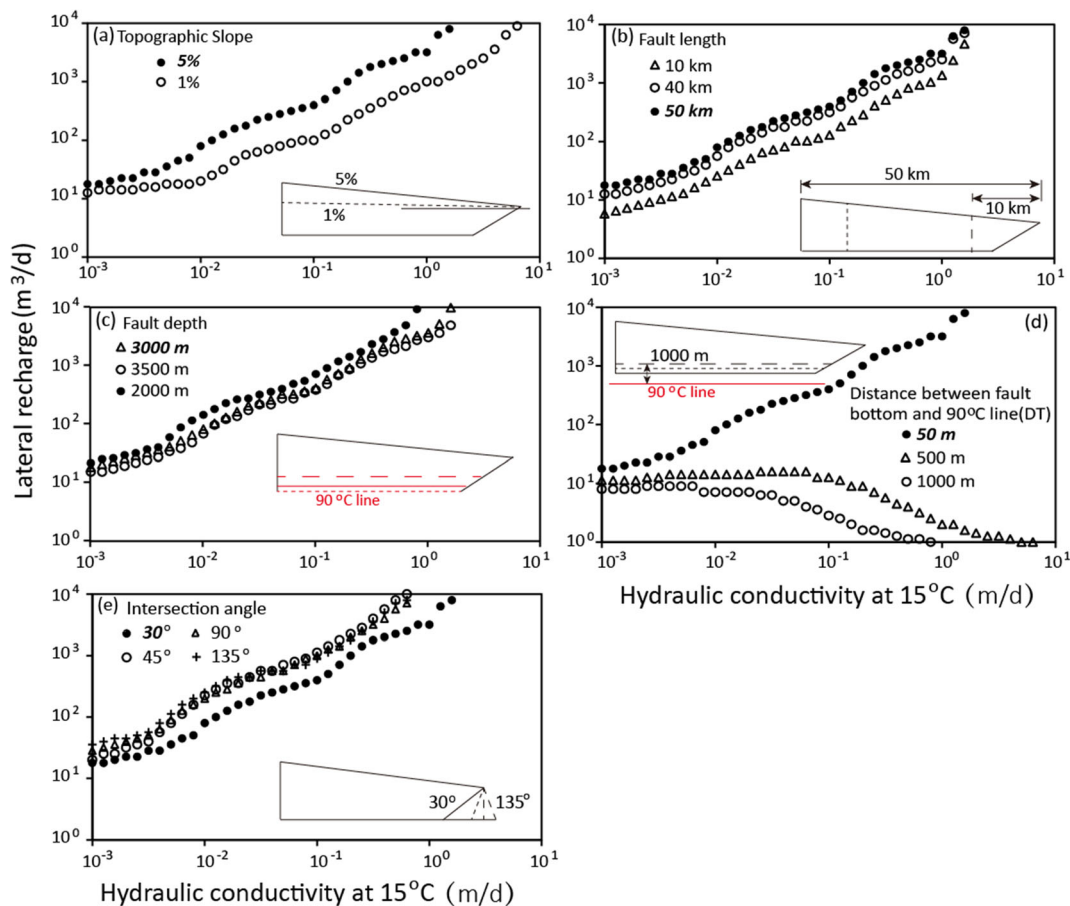


Fig. 5 The critical lines varying weakly with the **a** slope of the fault trace, **b** fault length, **c** fault depth and **e** intersection angle, but **d** strongly affected by the distance between the water circulation depth (or fault bottom) and the 90 °C line in the subsurface (DT), with the bold italic number representing the base case. In **c** the 90 °C line moves with the fault

bottom, while in **d** the 90 °C line is fixed at a depth of 3,000 m and the fault bottom is varied between depths of 2,950, 2,500 and 2,000 m, with the impermeable zone assigned between the fault bottom and the 90 °C line. In other words, in **c** the temperature at the fault bottom is fixed while in **d** the temperature at the fault bottom reduces with an increase of DT

and $K < 1$ m/day. If DT increases further, a geothermal spring cannot occur. CL30 in Fig. 5d can be fitted by second-order polynomials with correlation coefficients $>95\%$, leading to a CL cluster at different DT in Fig. 6.

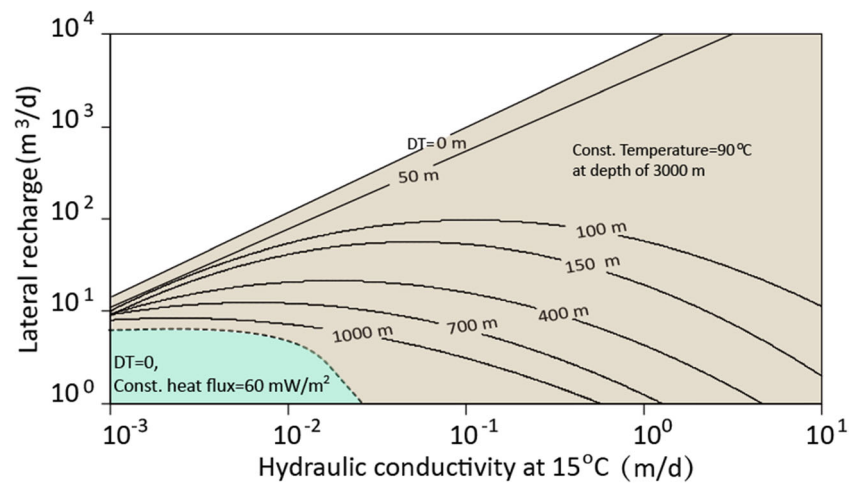
A sensitivity analysis was conducted to evaluate the possible influence of the thermal properties of the solid matrix on the outflow temperatures. As shown in Fig. 7a,b, the heat capacity and conductivity, which vary between shale, sandstone and granite, do not affect the position of the critical line and the outflow temperature. The thermal dispersivity has a larger influence on the CL30, but the influence is negligible when compared to that of DT.

Overall, CL30 in Fig. 6 is weakly affected by the fault length, intersection angles between faults, fault depth and thermal properties. Instead, CL30 quantitatively expresses the conditions of K , Q_L and DT for the formation of geothermal springs. A database expressing the relationship between K , Q_L , DT and spring temperature was then established based on 800 numerical simulations, which offer an additional reference to interpolate DT in the subsurface according to the

maximum discharge temperature and the total discharge rate of the spring, assuming that Q_L is determined by, e.g. geochemical or isotope analysis, and K in the fault damage zone is estimated according to the fracture density and aperture or inverse modeling. DT can be used to infer the depth of the 90 °C line once the maximum circulation depth of spring water was determined from the geochemical analysis, which helps to confirm whether geothermal resources exist at an economically viable depth. Moreover, if DT can be determined by the downhole logs, K or Q_L can be inferred from the observations of spring temperature as well.

Nine numerical examples are used to validate this method (Table 2; Fig. 8). Using N2 as an example, considering DT as unknown, and given the maximum temperature of 46 °C, and K and Q_L of 0.1 and 26 m³/day, respectively, DT can be evaluated by kriging based on the existing database. As a result, the DT value is estimated at 95 m, which fits well with the real DT value of 100 m with an error less than 5% (Fig. 8c). Similarly, Q_L is estimated given DT and K (Fig. 8a), and K is estimated given Q_L and DT (Fig. 8b). Overall, the estimated

Fig. 6 The contour lines of 30 °C under different distances between the maximum circulation depth and 90 °C line in the subsurface (DT), and also the contour lines of 30 °C inferred by using constant heat flux of 60 mW/m² at the fault bottom. The range of hydraulic conductivity and lateral recharge corresponding to the zone below each line represents the conditions for the occurrence of the geothermal spring. The effect of using a constant heat flux of 60 mW/m² at the model bottom is the same as that using the DT of about 1,500 m



parameters align well with the real values. However, at $K < 0.1$ m/day, a large error (about 50%) is presented. This is because the outflow temperature is less sensitive to K when K of the fault zone is low.

The method was then validated with the real data in the Guide Basin, northeastern Tibetan Plateau, China (Fig. 9a), where K values in the fault zone were estimated based on the measurements of the fracture density and aperture and inverse modeling. The subsurface temperature distribution was determined by the downhole logs, and the lateral recharge rate was estimated by the geochemical analysis and water budget calculation (Jiang et al. 2018). As a consequence, DT is estimated to be 80–100 m, given the K , Q_L and spring temperature, which follows well with downhole logs of

<100 m (Fig. 9b). K is estimated at 0.05 to 1 m/day, which is comparable to the values of 0.1 to 10 m/day calculated by previous work (Jiang et al. 2018).

Discussion

A constant temperature boundary was used at the bottom of the fault in this study instead of a constant heat flux boundary, assuming that the supportive heat from the earth interior is far larger than the heat extracted by the hydrologic cycle. The rationale of this assumption is illustrated in Fig. 10, which compares the heat flux at the fault bottom for the boundary conditions of constant temperature and constant heat flux,

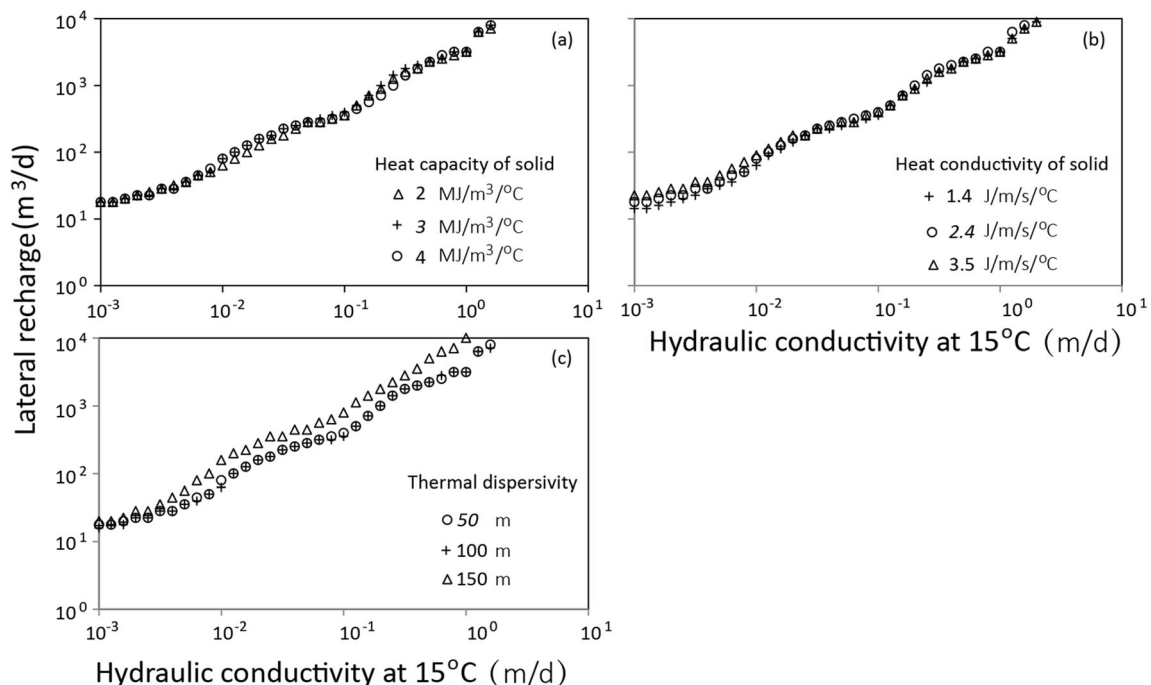


Fig. 7 The sensitivity of the critical line to **a** heat capacity, **b** heat conductivity of the solid and **c** thermal dispersivity

Table 2 Numerical examples and real geothermal parameters in the Guide Basin, China

ID	DT (m)	K (m/day)	Q_{total} (m ³ /day)	Q_L (m ³ /day)	T_{max} (°C)
N1	100	0.1	133.4	125.2	30
N2	100	0.1	46.5	26	46
N3	100	10	154.4	262	17
N4	50	1.0	1,163	1,061	47
N5	50	1.0	3,912	3,901	27
N6	50	0.1	333.4	331.7	30.4
N7	500	0.1	41.6	24.1	26.8
N8	500	1.0	264.1	60.1	17.4
N9	500	0.01	24.3	24.0	25
Guide Basin	<100	0.1–10	14	14	67

with hydraulic conductivity of 0.1 m/day, lateral recharge rate of 20 m³/day, and DT of 50 m. All the other hydraulic and thermal parameters are the same as those in base case (Table 1). It was calculated that under the constant-temperature boundary, the initial heat flux on the fault bottom is 60 mW/m²; however, when the temperatures and hydraulic heads reach steady state, the maximum heat flux at the fault bottom increases to almost 3 W/m². The conductive heat flux increases in the left part of the fault domain, because the inflow of cool water from the land surface reduces the system temperature, but increases the vertical temperature gradient at the fault bottom (Fig. 2a,b). This temperature gradient

decreases along the fault bottom with an increase in temperature, which leads the conductive heat flux to decrease accordingly, but increases the density contrast. As a consequence, the buoyancy enhances the vertical flow and thus the vertical density-driven heat flux. It is shown that the density-driven heat flux at the fault bottom exceeds the conductive flux at a horizontal distance of 3 km, which can contribute 90% of the heat flux at a distance of 30 km (Fig. 10).

When fixing the fault bottom heat flux (100% conductive heat) at 60 mW/m², insufficient heat is obtained by the fast convection of fluid flow driven by the lateral recharge and topography. Therefore, a much lower discharging temperature

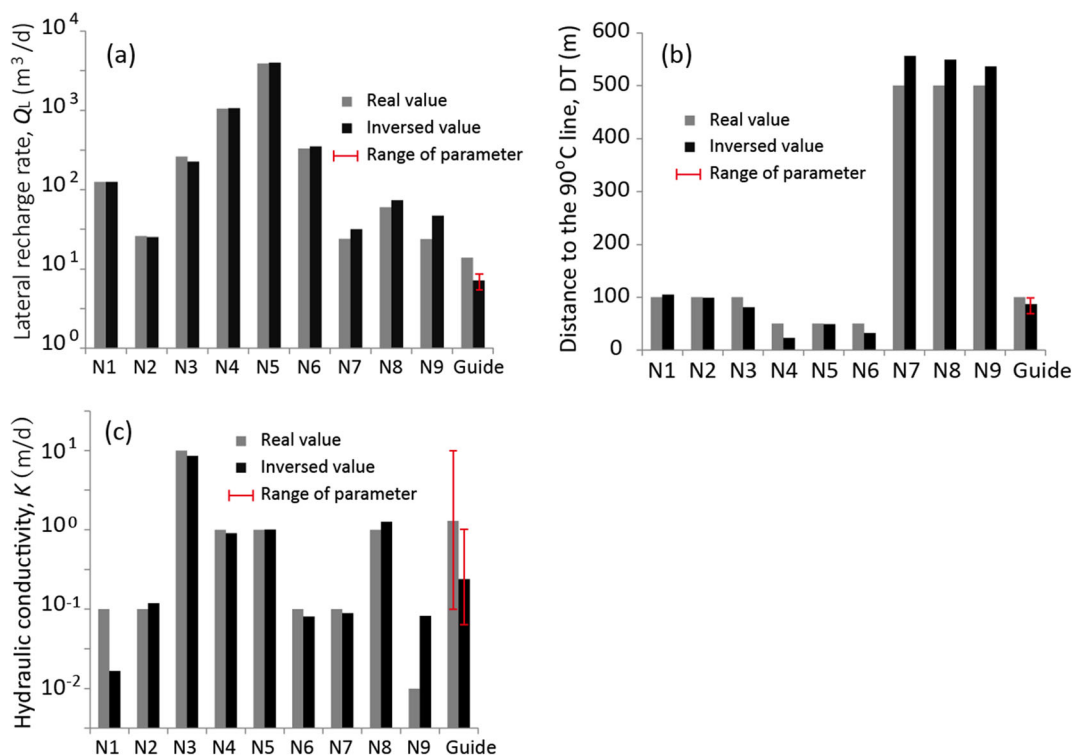


Fig. 8 The interpolation of **a** lateral recharge rate (Q_L), **b** distance between the circulation depth and the 90 °C line (DT), and **c** hydraulic conductivity in the fault zone (K) validated against numerical examples and real data in the Guide Basin, northeastern Tibetan plateau, China (in Table 2)

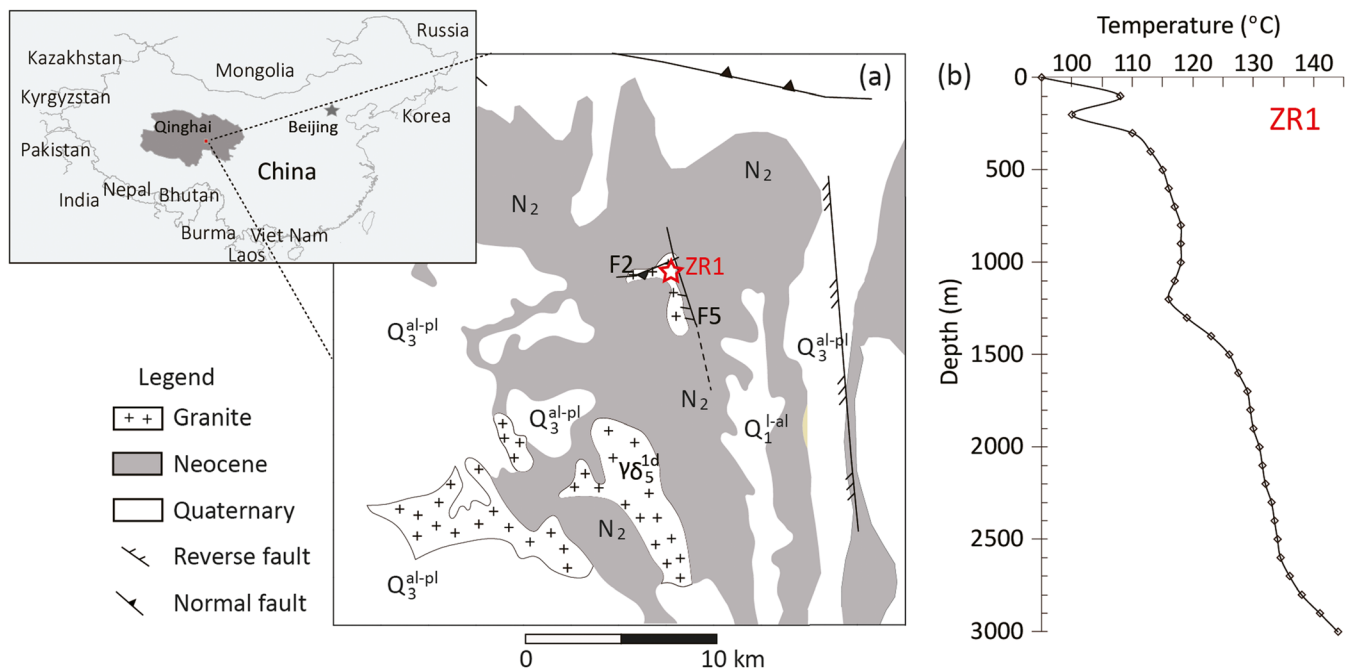


Fig. 9 **a** Geothermal spring created by conductive fault F2 and reverse impermeable fault F5 in the Guide Basin, Qinghai Province, China, and **b** a downhole temperature logs in drillhole ZR1 near the geothermal spring within a depth of 3,000 m (Jiang et al. 2018)

of 15.8 °C was obtained under the constant-heat flux boundary, when compared to the temperature of 55 °C under the constant temperature boundary. The contour line of 30 °C under constant heat flux of 60 mW/m² at the fault bottom was also established and illustrated in Fig. 6, which is comparable to the DT value of about 1,500 m.

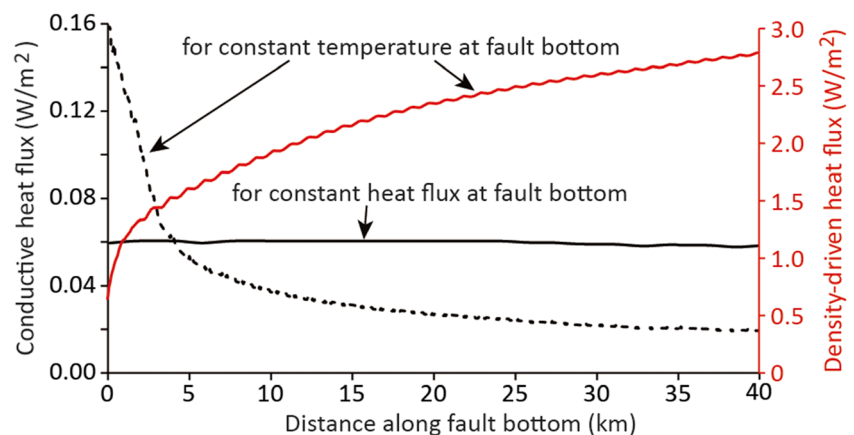
Recalling the situation in the Guide Basin in the northeastern Tibetan Plateau, the temperature at 3,000 m is measured at 150 °C (Fig. 9b), the conductive heat flux is about 60 mW/m², and the discharging temperature of the thermal spring reaches 67 °C. If a constant heat-flux is used, the conductive fault zone (F2 in Fig. 9a) is completely cooled down by the infiltration of the surface water. Instead, using a constant temperature boundary resulted in a sufficient spring temperature (Jiang et al. 2018); therefore, the constant-temperature boundary at the fault bottom was used in this 2D model.

Conclusion

This study revisited the conditions associated with the occurrences of geothermal springs in a fault zone. The following major conclusions are drawn:

1. The geothermal spring temperature and outflow rate are controlled by the lateral recharge rate from the country rock, the hydraulic conductivity of the fault damage zone and the distance between the fault bottom (or circulation depth of spring water) and the 90 °C line in the subsurface (DT). The influence of hydraulic conductivity is related to the strength of topography-driven flow along the fault plane, which represents the longest flow path and significantly influences the maximum spring temperature.

Fig. 10 Variations of heat flux at fault bottom by using a constant-temperature boundary and constant heat flux boundary



- The occurrence of a geothermal spring does not necessarily represent a geothermal anomaly in the subsurface. In a normal geothermal background (with the geothermal gradient equal to, or even lower than, the global average value), geothermal springs can occur at suitable conditions of lateral recharge, hydraulic conductivity and DT. Through numerical simulations, a database was established expressing the relationship between spring temperature, fault hydraulic conductivity, lateral recharge rate and DT, and the contour line of 30 °C, to quantitatively express the conditions associated with geothermal spring occurrence.
- The database offered a reference for interpolating DT in the fault zone, once the lateral recharge rate to the fault and hydraulic conductivity have been evaluated. This can be further used to determine the depth of the high-temperature reservoir after the circulation depth of spring water was estimated. By fixing any two of DT, hydraulic conductivity and lateral recharge rate, the third component can be estimated from the spring temperature.

Acknowledgements We thank Christoph Schrank and Daniel Owen from Queensland University of Technology, Australia, and three reviewers for their constructive suggestions, which helped improving this article.

Funding Information Funding support for this study was provided by National Natural Science Foundation of China (Nos. 41502222 and 41572215), China Postdoctoral Science Foundation funding (No. 2016 M591483), and the Geological Survey project in Qinghai Province (No. 121201012000150011). This study was also supported by the International Postdoctoral Exchange Fellowship Program (2017) from China Postdoctoral Council.

Appendix: Theoretical background of flow and heat transport in fault zone

The mass balance for groundwater flow in porous media is described as (Diersch and Kolditz 2009):

$$S \frac{\partial h}{\partial t} + \frac{\partial q_x}{\partial x} + \frac{\partial q_z}{\partial z} = 0, \quad q_x = -K f_\mu \frac{\partial h}{\partial x}, \quad q_z = -K f_\mu \left(\frac{\partial h}{\partial z} + \frac{\rho_f - \rho_{f_0}}{\rho_{f_0}} \right), \quad (1)$$

where h is the hydraulic head (m), q is the flow velocity (m/day), S is the storage coefficient, K is the hydraulic conductivity, ρ is the water density (kg/m^3), and f_μ is a temperature factor that controls the variation of hydraulic conductivity and viscosity:

$$f_\mu = \frac{1 + 0.7063\zeta_0 - 0.04832\zeta_0^3}{1 + 0.7063\zeta - 0.04832\zeta^3}, \quad \zeta_0 = \frac{T_0 - 150}{100}, \quad \zeta = \frac{T - 150}{100}, \quad (2)$$

The energy balance of the heat transport via conduction and convection is governed by:

$$\begin{aligned} & [\phi C_f + (1-\phi)C_s] \frac{\partial T}{\partial t} \\ & + C_f \left(q_x \frac{\partial T}{\partial x} + q_z \frac{\partial T}{\partial z} \right) - \lambda \left(\frac{\partial^2 T}{\partial x^2} + \frac{\partial^2 T}{\partial z^2} \right) \\ & = 0, \end{aligned} \quad (3)$$

where ϕ is the porosity, C_f is the heat capacity of water, C_s is the heat capacity of country rock ($\text{MJ/m}^3 \text{ } ^\circ\text{C}$), T is temperature ($^\circ\text{C}$), λ is the heat conductivity ($\text{W/m } ^\circ\text{C}$) that is composed by solid and fluid parts:

$$\lambda_b = \phi \lambda_f + (1-\phi) \lambda_s \quad (4)$$

where λ_f and λ_s are the heat conductivity of solid and fluid, respectively.

References

- Ball LB, Caine JS, Ge S (2014) Controls on groundwater flow in a semiarid folded and faulted intermountain basin. *Water Resour Res* 50:6788–6809. <https://doi.org/10.1002/2013WR014451>
- Barka A, Kadinsky-Cade K (1988) Strike-slip fault geometry in Turkey and its influence on earthquake activity. *Tectonics* 7:663–684
- Bense V, Person M (2006) Faults as conduit-barrier systems to fluid flow in siliciclastic sedimentary aquifers. *Water Resour Res* 42(5). <https://doi.org/10.1029/2005WR004480>
- Bense V, Gleeson T, Loveless S, Bour O, Scibek J (2013) Fault zone hydrogeology. *Earth Sci Rev* 127:171–192
- Boyle G (1997) Renewable energy: power for a sustainable future. Oxford University Press in association with The Open University, Oxford, UK
- Bucher K, Zhang L, Stober I (2009) A hot spring in granite of the western Tianshan, China. *Appl Geochem* 24:402–410
- Cappa F, Rutqvist J (2011) Modeling of coupled deformation and permeability evolution during fault reactivation induced by deep underground injection of CO_2 . *Int J Greenhouse Gas Control* 5:336–346. <https://doi.org/10.1016/j.ijggc.2010.08.005>
- Chapman DS (1986) Thermal gradients in the continental crust. *Geol Soc Lond Spec Publ* 24:63–70. <https://doi.org/10.1144/gsl.sp.1986.024.01.07>
- Christensen NI, Mooney WD (1995) Seismic velocity structure and composition of the continental crust: a global view. *J Geophys Res Solid Earth* 100:9761–9788. <https://doi.org/10.1029/95JB00259>
- Curewitz D, Karson JA (1997) Structural settings of hydrothermal outflow: fracture permeability maintained by fault propagation and interaction. *J Volcanol Geotherm Res* 79:149–168. [https://doi.org/10.1016/S0377-0273\(97\)00027-9](https://doi.org/10.1016/S0377-0273(97)00027-9)
- Diersch HJ (2013) FEFLOW: finite element modeling of flow, mass and heat transport in porous and fractured media. Springer, Heidelberg, Germany
- Diersch HJG, Kolditz O (2009) Coupled groundwater flow and transport: thermohaline and 3D convection systems. FEFLOW White Papers 1, WASY, Berlin, pp 315–358
- Evans JP, Forster CB, Goddard JV (1997) Permeability of fault-related rocks, and implications for hydraulic structure of fault zones. *J Struct*

- Geol 19:1393–1404. [https://doi.org/10.1016/S0191-8141\(97\)00057-6](https://doi.org/10.1016/S0191-8141(97)00057-6)
- Fairley JP (2009) Modeling fluid flow in a heterogeneous, fault-controlled hydrothermal system. *Geofluids* 9:153–166. <https://doi.org/10.1111/j.1468-8123.2008.00236.x>
- Fairley JP, Hinds JJ (2004) Rapid transport pathways for geothermal fluids in an active Great Basin fault zone. *Geology* 32:825–828. <https://doi.org/10.1130/g20617.1>
- Forster C, Smith L (1989) The influence of groundwater flow on thermal regimes in mountainous terrain: a model study. *J Geophys Res Solid Earth* 94:9439–9451. <https://doi.org/10.1029/JB094iB07p09439>
- Ji Y, Yoshioka S, Matsumoto T (2016) Three-dimensional numerical modeling of temperature and mantle flow fields associated with subduction of the Philippine Sea plate, Southwest Japan. *J Geophys Res Solid Earth* 121:4458–4482. <https://doi.org/10.1002/2016JB012912>
- Jiang Z, Xu T, Owen DDR, Jia X, Feng B, Zhang Y (2018) Geothermal fluid circulation in the Guide Basin of the northeastern Tibetan plateau: isotopic analysis and numerical modeling. *Geothermics* 71: 234–244
- Judson S, Kauffman ME, Leet LD (1987) *Physical geology*. Prentice Hall, Upper Saddle River, NJ
- Karrech A, Schrank C, Freij-Ayoub R, Regenauer-Lieb K (2014) A multi-scaling approach to predict hydraulic damage of poromaterials. *Int J Mech Sci* 78:1–7. <https://doi.org/10.1016/j.ijmecsci.2013.10.010>
- López DL, Smith L (1995) Fluid flow in fault zones: analysis of the interplay of convective circulation and topographically driven groundwater flow. *Water Resour Res* 31:1489–1503
- Lund JW, Freeston DH, Boyd TL (2011) Direct utilization of geothermal energy 2010 worldwide review. *Geothermics* 40:159–180. <https://doi.org/10.1016/j.geothermics.2011.07.004>
- Mádl-Szőnyi J, Tóth Á (2015) Basin-scale conceptual groundwater flow model for an unconfined and confined thick carbonate region. *Hydrogeol J* 23:1359–1380. <https://doi.org/10.1007/s10040-015-1274-x>
- Magri F, Möller S, Inbar N, Möller P, Raggad M, Rödiger T, Rosenthal E, Siebert C (2016) 2D and 3D coexisting modes of thermal convection in fractured hydrothermal systems: implications for transboundary flow in the Lower Yarmouk Gorge. *Mar Pet Geol* 78:750–758. <https://doi.org/10.1016/j.marpetgeo.2016.10.002>
- Malkovsky VI, Magri F (2016) Thermal convection of temperature-dependent viscous fluids within three-dimensional faulted geothermal systems: estimation from linear and numerical analyses. *Water Resour Res* 52:2855–2867. <https://doi.org/10.1002/2015WR018001>
- Murphy HD (1979) Convective instabilities in vertical fractures and faults. *J Geophys Res Solid Earth* 84:6121–6130
- Peacock D, Sanderson D (1992) Effects of layering and anisotropy on fault geometry. *J Geol Soc* 149:793–802
- Pentecost A, Jones B, Renaut R (2003) What is a hot spring? *Can J Earth Sci* 40:1443–1446
- Saffer DM, Bekins BA, Hickman S (2003) Topographically driven groundwater flow and the San Andreas heat flow paradox revisited. *J Geophys Res Solid Earth* 108:ETG12. <https://doi.org/10.1029/2002JB001849>
- Smith DA (1980) Sealing and nonsealing faults in Louisiana Gulf Coast salt basin. *AAPG Bull* 64:145–172
- Sorey ML (1975) Numerical modeling of liquid geothermal systems. US Government Printing Office, Washington, DC, 60 pp
- Sorey ML (1985) Evolution and present state of the hydrothermal system in Long Valley Caldera. *J Geophys Res Solid Earth* 90:11219–11228
- Stober I, Zhong J, Zhang L, Bucher K (2016) Deep hydrothermal fluid–rock interaction: the thermal springs of Da Qaidam, China. *Geofluids* 16:711–728
- Wibberley CA, Yielding G, Di Toro G (2008) Recent advances in the understanding of fault zone internal structure: a review. *Geol Soc Lond Spec Publ* 299:5–33
- Younger PL (2014) Missing a trick in geothermal exploration. *Nat Geosci* 7:479–480. <https://doi.org/10.1038/ngeo2193>